The Astrophysical Journal Letters, 864:L34 (7pp), 2018 September 10 https://doi.org/10.3847/2041-8213/aaddf6

An Unusual Energetic Particle Flux Enhancement Associated with Solar Wind Magnetic Island Dynamics

L.-L. Zhao[1], G. P. Zank[1,2,4], O. Khabarova[3], S. Du[2], Y. Chen[2], L. Adhikari[1], and Q. Hu[1,2]
[1] Center for Space Plasma and Aeronomic Research (CSPAR), University of Alabama in Huntsville, Huntsville, AL 35805, USA
[2] Department of Space Science, University of Alabama in Huntsville, Huntsville, AL 35899, USA
[3] Heliophysical Laboratory, Pushkov Institute of Terrestrial Magnetism, Ionosphere and Radio Wave Propagation of the Russian Academy of Sciences (IZMIRAN), Moscow 142190, Russia
Received 2018 June 23; revised 2018 August 27; accepted 2018 August 29; published 2018 September 11

Abstract

The possibility that charged particles are accelerated statistically in a "sea" of small-scale interacting magnetic flux ropes in the supersonic solar wind is gaining credence. In this Letter, we extend the Zank et al. statistical transport theory for a nearly isotopic particle distribution by including an escape term corresponding to particle loss from a finite acceleration region. Steady-state 1D solutions for both the accelerated particle velocity distribution function and differential intensity are derived. We show *Ulysses* observations of an energetic particle flux enhancement event downstream of a shock near 5 au that is inconsistent with the predictions of classical diffusive shock acceleration (DSA) but may be explained by local acceleration associated with magnetic islands. An automated Grad-Shafranov reconstruction approach is employed to identify small-scale magnetic flux ropes behind the shock. For the first time, the observed energetic particle "time-intensity" profile and spectra are quantitatively compared with theoretical predictions. The results show that stochastic acceleration by interacting magnetic islands accounts successfully for the observed (i) peaking of particle intensities behind the shock instead of at the shock front as standard DSA predicts; (ii) increase in the particle flux amplification factor with increasing particle energy; (ii) increase in distance between the particle intensity peak and the shock front with increasing energy; and (iv) hardening of particle power-law spectra with increasing distance downstream of the shock.

Key words: acceleration of particles – magnetic reconnection – shock waves – solar wind

1. Introduction

Small-scale magnetic flux ropes are coherent quasi-2D nonlinear structures possessing a twist, or islands with an out-of-plane axial or guide magnetic field component, and are advected with the large-scale flow. Dynamically interacting magnetic flux ropes or islands are an emerging paradigm for the energization of charged particles throughout the heliosphere. Recent studies suggest that the observed unusual energetic particle flux enhancements at the leading edge of interplanetary coronal mass ejections, downstream of interplanetary shocks and near the heliospheric current sheet (HCS) might be related to local acceleration in regions filled with numerous active magnetic islands (Chian & Muñoz 2011; Zank et al. 2014, 2015; Khabarova et al. 2015a, 2015b, 2016, 2017; le Roux et al. 2015, 2016; Khabarova & Zank 2017).

The generation of small-scale magnetic flux ropes is intrinsic to quasi-2D magnetohydrodynamic (MHD) turbulence—a dominant component of solar wind turbulence suggested by observations (Matthaeus et al. 1990; Bieber et al. 1996), nearly incompressible MHD models (Zank & Matthaeus 1992, 1993; Hunana & Zank 2010; Zank et al. 2017), and simulations of decaying MHD turbulence (Dmitruk et al. 2004; Greco et al. 2009; Servidio et al. 2009, 2010). Recently, Zheng & Hu (2018) identify small-scale magnetic flux ropes associated with intermittent solar wind turbulence. Moreover, Khabarova et al. (2015a, 2015b, 2016) suggest that the disturbed HCS generates small-scale magnetic islands in its neighborhood.

Early (Matthaeus et al. 1984; Ambrosiano et al. 1988) and subsequent simulations indicate that charged particle acceleration in turbulent MHD fields with multiple magnetic islands is possible (e.g., Drake et al. 2006a, 2006b, 2013; Oka et al. 2010; Hoshino 2012; Le et al. 2012). From these studies, three different mechanisms are thought to play an important role in the energization of charged particles propagating in a dynamical "sea" of magnetic islands. First, particles trapped in a contracting compressible island experience repeated "converging" reflections, thus gaining energy via a first-order Fermi process. Second, particles can be energized through second-order Fermi acceleration due to the shortening of the magnetic field lines as two magnetic islands merge incompressibly. Third, partially trapped particles can be accelerated by interacting repeatedly with the reconnection electric field generated by island merging.

Zank et al. (2014, henceforth Z2014) and le Roux et al. (2015) combined these three acceleration processes to develop a stochastic transport theory for charged particles propagating in a turbulent region filled with numerous interacting small-scale flux ropes. In solving the gyrophase-averaged transport equation for a nearly isotropic particle distribution, Z2014 neglected the second-order Fermi acceleration for simplicity. The ab initio Zank et al. (2014) and le Roux et al. (2015) theories showed that reconnection processes associated with magnetic islands can accelerate charged particles and produce power-law-like distributions.

Particle energization up to MeV energies that is inconsistent with classical diffusive shock acceleration (DSA) has been ascribed to magnetic island dynamics, both at 1 au and in the outer heliosphere (e.g., Tessein et al. 2013, 2015, 2016; Khabarova et al. 2015a, 2015b, 2016; Zank et al. 2015; Khabarova & Zank 2017). However, no direct quantitative comparison between theoretical solutions and the observed

[4] Corresponding author.

energetic particle distributions has been made. In this Letter, we report unusual energetic particle events observed by *Ulysses* near 5 au. An automated approach based on the Grad–Shafranov (GS) reconstruction technique (Sonnerup & Guo 1996; Hau & Sonnerup 1999; Hu 2017) is employed to detect numerous small-scale magnetic islands downstream of the associated shock. We further introduce an escape term to the Z2014 nearly isotropic transport theory and use it to explain the observed particle "time-intensity" profile and the evolution of spectra.

2. Particle Acceleration by Magnetic Island Dynamics

To describe particle escape (or loss) in the diffusion-convection equation derived in Z2014, we introduce a simple escape term

$$\left.\frac{df}{dt}\right)_{\rm esc} = -\frac{f}{\tau_e}, \tag{1}$$

where f is the nearly isotropic particle distribution function and τ_e is the particle escape time (assumed as a constant). The modified 1D steady-state transport equation becomes

$$\frac{\partial^2 f}{\partial x^2} - 2\frac{V_E}{\kappa}\frac{\partial^2 f}{\partial x \partial \xi} - \frac{U+3V_E}{\kappa}\frac{\partial f}{\partial x} - \frac{2\eta_c}{3\kappa}\frac{\partial f}{\partial \xi} - \frac{2\eta_c}{\kappa} f = -\frac{Q}{\kappa} v_0 \delta(v - v_0)\delta(x) + \frac{f}{\kappa\tau_e}, \tag{2}$$

where $\xi = \ln(v/v_0)$, v is the particle velocity, and v_0 is the injection velocity. Equation (2) includes the large-scale super-Alfvénic flow speed, U, a scattered anti-reconnection electric field velocity, V_E, the spatial diffusion coefficient, κ, and the magnetic island contraction rate, η_c. A normalization factor is defined as $Q = n_0/(4\pi v_0^2)$, where n_0 is the particle number density. Equation (2) corresponds to Equation (35) in Z2014, now with the additional escape term. The delta functions indicate mono-energetic injection of particles at $x = 0$, which provides a jump condition across the injection point. The equation can be solved analytically by assuming that all parameters (U, V_E, τ_e, κ, and η_c) are homogeneous in time and space, and are energy independent. Following Z2014, we introduce a Laplace transform in the variable ξ, $\bar{f}(x, s) = \mathcal{L}[f(x, \xi)]$, which reduces (2) to

$$\begin{aligned} &\frac{d^2\bar{f}}{dx^2} - \frac{g(s)}{\kappa}\frac{d\bar{f}}{dx} - \frac{h(s)}{k}\bar{f} - \frac{\bar{f}}{\kappa\tau_e} = -\frac{Q}{\kappa}\delta(x); \\ &g(s) \equiv U + 3V_E + 2V_E s; \\ &h(s) \equiv \frac{2\eta_c}{3}(s+3). \end{aligned} \tag{3}$$

The complementary solution to Equation (3) is

$$\bar{f}(x, s) = \frac{Q}{\kappa\sqrt{\Delta}} \begin{cases} e^{\lambda_1 x}, & x > 0, \quad \lambda_1 = \dfrac{g(s)}{2\kappa} - \dfrac{\sqrt{\Delta}}{2} \\ e^{\lambda_2 x}, & x < 0, \quad \lambda_1 = \dfrac{g(s)}{2\kappa} + \dfrac{\sqrt{\Delta}}{2} \end{cases}; \tag{4}$$

$$\kappa\sqrt{\Delta} = 2V_E\left[(s - s_1)^2 - \frac{\eta_c\kappa}{3V_E^3}\left(U - 3V_E + \frac{\eta_c\kappa}{3V_E}\right) + \frac{\kappa}{\tau_e V_E^2}\right]^{1/2};$$

$$s_1 = -\frac{1}{2}\left(\frac{U+3V_E}{V_E} + \frac{2\eta_c\kappa}{3V_E^2}\right).$$

The inverse Laplace transform of Equation (4) yields the solution for the particle velocity distribution function

$$\begin{aligned} f\left(x, \frac{v}{v_0}\right) = {} & \frac{n_0}{8\pi v_0^2 V_E}\left(\frac{v}{v_0}\right)^{-(3+M_E+2\tau_d/(3\tau_c)M_E^2)/2} \\ & \times \exp\left[-\frac{\tau_d}{3\tau_c}M_E\frac{x}{L_{\rm diff}}\right] \\ & \times I_0(\Phi) H\left(\ln\left(\frac{v}{v_0}\right)\right) H\left[\ln\left(\frac{v}{v_0}\right) + \frac{1}{M_E}\frac{x}{L_{\rm diff}}\right]; \end{aligned} \tag{5}$$

$$\Phi = \sqrt{\frac{\tau_d}{3\tau_c}M_E^2\left(M_E - 3 + \frac{\tau_d}{3\tau_c}M_E^2\right) - \frac{\tau_d}{\tau_e}M_E} \times \left[\ln^2\left(\frac{v}{v_0}\right) + \frac{2}{M_E}\ln\left(\frac{v}{v_0}\right)\frac{x}{L_{\rm diff}}\right]^{1/2},$$

where $\tau_c = 1/\eta_c$ is the characteristic island contraction time, $\tau_d = \kappa/U^2$ is the characteristic particle diffusion time, $L_{\rm diff} = \kappa/U$ is the diffusion length scale, $M_E = U/V_E$ is a dimensionless parameter that characterizes the strength of the anti-reconnection electric field, and I_0 denotes the zero-order modified Bessel function of the first kind.

Figure 1 shows several examples of the solutions of Equation (5) for two values of τ_d/τ_c and four values of τ_d/τ_e. The solutions are normalized to $f_0 = f(v/v_0 = 1)$ and evaluated at a fixed location $x/L_{\rm diff} = 1$. For all cases, the spectrum is essentially a power law. Efficient particle escape corresponds to a small escape time τ_e or a large τ_d/τ_e value. Figure 1 shows that a larger τ_d/τ_e value produces a steeper spectrum, which is a natural consequence of particle escape.

3. Overview of the Observations

Figure 2 shows the observed energetic proton fluxes, together with the plasma and magnetic field parameters during the period of 2004 February 13 00:00 UT to 2004 February 21 02:00 UT. Panel (a) shows the energetic proton flux measured by the *Ulysses* LEMS30 detector in the eight energy channels listed. Panels (b)–(e) show, respectively, the magnetic field, proton speed and temperature, proton number density, and proton beta. During this period, *Ulysses* crossed the heliographic equator at 5.36 au. An interplanetary shock (dashed vertical line) was detected at 15:15:27 UT on 2004 February 14, being a fast forward shock with a compression ratio of $r = 2.5$ (http://ipshocks.fi/database). Previous studies suggest that shocks may create favorable downstream conditions for particle acceleration, such as the production and confinement of magnetic islands (Zank et al. 2015; Khabarova et al. 2016; le Roux et al. 2016). Using the GS reconstruction technique, we identify 31 magnetic flux rope structures during the considered

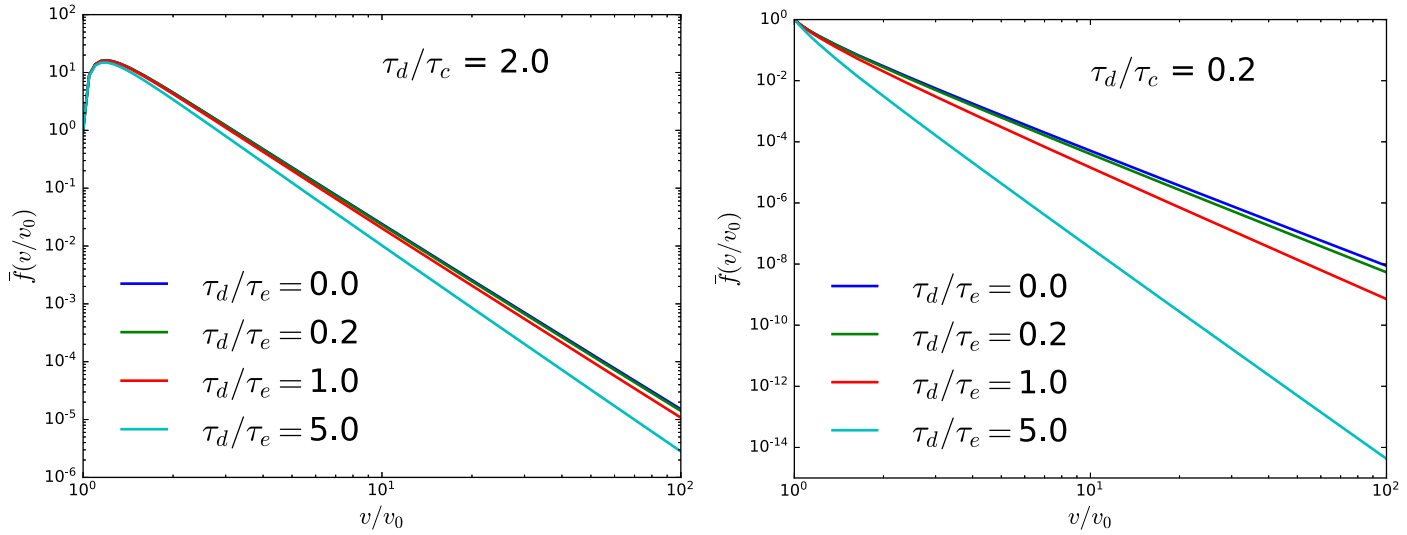

Figure 1. Normalized solution of Equation (5) at a fixed spatial location of $x/L_{\rm diff} = 1$. The two panels show solutions with $\tau_d/\tau_c = 2.0$ and 0.2, respectively. We choose four different τ_d/τ_e values: 0, 0.2, 1.0, and 5.0. The solutions are normalized to $f_0 = f(v/v_0 = 1)$, and $M_E = 10$ is assumed in all cases.

time period, marked as the shaded areas in the figure. The reconstructed flux ropes have durations ranging from 46 to 949 minutes, sizes from 0.0048 to 0.19 au, and mean magnetic field from 0.025 to 2.29 nT. The GS reconstructed cross-section maps (i.e., Teh et al. 2009; Hietala et al. 2014) for selected flux rope intervals are shown in the bottom of Figure 2. In each map, the black contour lines are the projection of flux surfaces onto the x–y plane perpendicular to the flux rope axis, z. The axial field component B_z (indicated by colors) usually reaches maximum near the flux rope center (marked by the white dot) and decreases monotonically toward the edge. Therefore, the field line configuration comprises a straight central field line along the z axis and spiral field lines winding around, lying on distinct flux surfaces, clearly indicative of a flux rope configuration. The inputs for the GS reconstruction include both magnetic field and plasma measurements, from which the z axis orientation and the frame velocity comoving with the structure are determined. *Ulysses* crossed the structure along $y = 0$ on the map where the white arrows represent measured transverse magnetic field. Various parameters can be readily obtained from these maps. For example, the structure in the left map has a scale size of ~0.05 au, maximum axial field strength ~2.6 nT, and right-hand chirality.

4. Modeling the Particle Flux Amplification

We use Equation (5) to model the observed post-shock energetic proton flux enhancement. Figure 2 shows that the low-energy particle fluxes are strongly enhanced at the shock front, and decrease rapidly after the shock passage. This spike-like feature in particle intensity during the shock passage indicates an energetic storm particle event (Bryant et al. 1962), and is energy dependent (Reames 1995). The DSA-attributed energetic particle flux often forms an almost symmetric peak at the shock (Neugebauer et al. 2006; Tessein et al. 2015). Here, we do not address the rapid changes in low-energy particle intensities during the passage of the shock but focus exclusively on the acceleration of particles further downstream of the shock. Classical DSA theory predicts that the particle intensity downstream of the shock is constant with distance. From the top panel of Figure 2, the downstream proton intensities depart significantly from the predictions of DSA since the flux of each energy channel is amplified relative to its value at the shock, except for the two lowest energy channels. High-energy particle (>130 keV) fluxes peak at about 2–3 days after the shock passage.

To model the observed flux amplification using the solution from Equation (5), we need determine the particle injection point. Here, we choose a point ~12 hr behind the shock (at 03:00 UT 2004 February 15) where particle intensities are near a local minimum (Tessein et al. 2016). This injection point is approximately equivalent to 2–3 times the integral scale of turbulence downstream of the shock (Adhikari et al. 2017; Zank et al. 2017; Zhao et al. 2017, 2018), and it is also characterized by abrupt changes in the magnetic field direction (Figure 2(b)), which signals the formation of strong current sheets. After the crossing of the injection region, particles interact primarily with magnetic islands and cannot propagate back to the quasi-perpendicular shock ($\theta_{\rm Bn} \sim 50°$) front easily. Locating the injection point a short distance downstream allows us to eliminate the DSA-attributed effect and examine particle acceleration via flux rope-related processes.

Figure 3 shows the theoretical solution of Equation (5) with the observed particle flux amplification overplotted as dashed lines (the flux rope intervals are also marked). The boundary of the acceleration region is chosen at 00:00 UT 2004 February 21 (corresponding to $x/L_{\rm diff} = 82.25$), where the observed low-energy particle fluxes return to quiet levels. Both the analytic solutions and data are normalized to the values at the injection position $x = 0$ (dotted–dashed vertical line). A physical derivation of the model parameters requires knowledge of the magnetic island dynamics such as the contraction and reconnection rate, and is not easily attainable. Although the typical size of flux ropes can be associated with the 2D turbulence outerscale (Matthaeus et al. 1999), which is useful for gaining information of the 2D turbulence spectrum at a low wavenumber, hence the particle diffusion coefficient (Matthaeus et al. 2007), this is still under investigation. Therefore, all model parameters here are derived from fitting to the observed particle flux. The trial-and-error fitting is done by adjusting the dimensionless parameters M_E, τ_d/τ_c, τ_d/τ_e, and v_1/v_0. The particle velocity v is calculated as an average velocity in their corresponding energy range, and v_1 is the

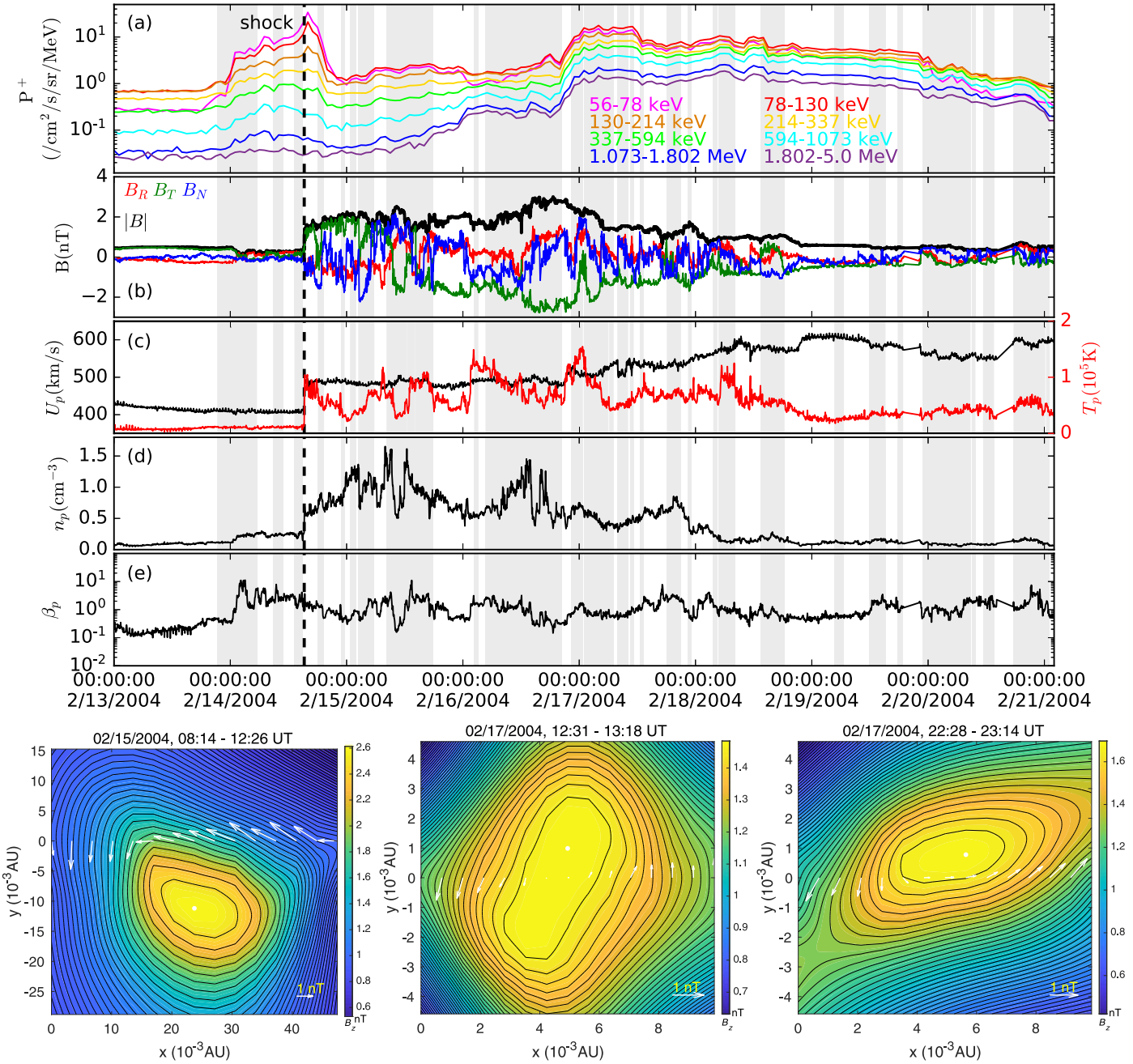

Figure 2. Top five panels: parameters from the *Ulysses* measurement including (a) 1 hr resolution energetic proton fluxes measured by the LEMS30 detector for the eight energy channels listed in the figure; (b) components and magnitiude of the magnetic field; (c) solar wind proton speed and temperature; (d) proton number density; and (e) proton beta. The dashed vertical line identifies the location of an interplanetary shock. Shaded areas are the GS reconstructed magnetic flux ropes. The selected cross-section maps from GS reconstruction are shown in the bottom.

velocity corresponding to the lowest energy channel. To convert the time series data to the spatial coordinate (x), we assume a constant flow velocity of $U_{\rm flow} = 480\,{\rm km\,s^{-1}}$, which is the observed solar wind speed during this period. The spatial coordinate x is normalized by the diffusion length $L_{\rm diff}$. The set of best-fit parameters is $M_E = 10$, $\tau_d/\tau_c = 0.10$, $\tau_d/\tau_e = 0.15$, $v_1/v_0 = 20$, and $L_{\rm diff} = 3.0 \times 10^{11}$ cm.

Figure 3 shows clearly that the particle intensities are strongly enhanced with respect to the injection position for an extended period (~5 days), and the enhancement is more pronounced for high-energy particles. The largest amplification is about 10 times for the 56–78 keV energy range and 70 times for the 1.802–5 MeV energy range. The amplification factor is in ascending order with increasing energy. The distance between the particle flux peak and the injection point appears to increase with increasing energy. For example, the flux amplification peaks at $x/L_{\rm diff} \sim 27$ for the 56–78 keV range and at $x/L_{\rm diff} \sim 44$ for the 1.802–5.0 MeV range. These features are quantitatively reproduced by our analytic model. The particle behavior at late times (corresponding to $x/L_{\rm diff} \sim 25$–80) closely follows the model prediction for all considered energy channels.

While the model reproduces the primary intensity features, it certainly does not capture every observed detail. For example, the flux amplification in the region $x/L_{\rm diff} \sim 0$–25 is smaller than the model prediction, especially for low-energy particles.

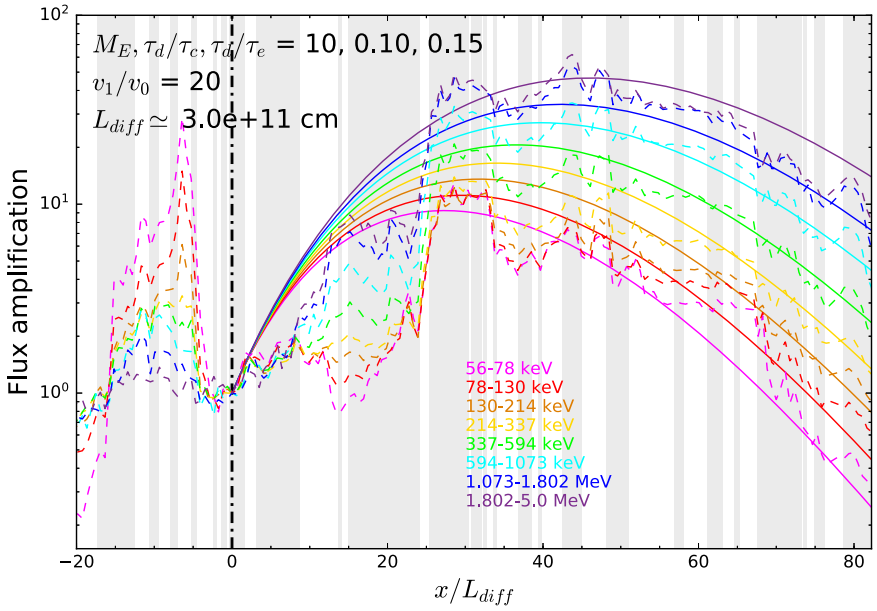

Figure 3. Particle flux amplification factor as a function of position. The dotted–dashed vertical line identifies the particle injection point (at 03:00 UT 2004 February 15). Both the observed fluxes and the theoretical distribution functions are normalized to their respective values at the injection point. Dashed lines of different colors denote the observed proton flux amplification factor. Solid lines show the theoretical amplification factor $f(x, v/v_0)/f(0, v/v_0)$ obtained from Equation (5) for the corresponding energy channel. Shaded areas identify flux ropes. Parameters used in Equation (5) are shown in the figure.

One reason may be that we neglect the spatial variation of flux rope dynamics. The early-time region may correspond to an initial island formation and growth phase, and, being less active dynamically, leads to less efficient energization than what occurs further downstream in a fully developed "sea" of dynamically interacting islands where the Z2014 theory is fully applicable.

5. Spectra of Accelerated Particles

Consider now the downstream energetic particle spectra for this event. To directly compare with the observations, we convert our theoretical velocity distribution function, f, to the particle differential intensity, $j(E)$, using

$$j(E) = \frac{2E}{m^2} f\left(\sqrt{\frac{2E}{m}}\right), \tag{6}$$

where E is the particle energy. Since our particle velocity, v, is normalized to the injection velocity, v_0, we normalize the energy to the corresponding injection energy, E_0. The differential intensity corresponding to Equation (5) is then

$$j\left(x, \frac{E}{E_0}\right) = j_0 \left(\sqrt{\frac{E}{E_0}}\right)^{-(3+M_E+2\tau_d/(3\tau_c)M_E^2)/2} \times \frac{E}{E_0} \exp\left[-\frac{\tau_d}{3\tau_c} M_E \frac{x}{L_{\rm diff}}\right] \times I_0(\Phi) H\left(\ln\left(\sqrt{\frac{E}{E_0}}\right)\right) H\left[\ln\sqrt{\frac{E}{E_0}} + \frac{1}{M_E}\frac{x}{L_{\rm diff}}\right]; \tag{7}$$

$$\Phi = \sqrt{\frac{\tau_d}{3\tau_c} M_E^2 \left(M_E - 3 + \frac{\tau_d}{3\tau_c} M_E^2\right) - \frac{\tau_d}{\tau_e} M_E} \times \left[\left(\ln\sqrt{\frac{E}{E_0}}\right)^2 + \frac{2}{M_E} \ln\sqrt{\frac{E}{E_0}} \frac{x}{L_{\rm diff}}\right]^{1/2},$$

where j_0 is a normalization factor. The values of M_E, τ_d/τ_c, τ_d/τ_e, and $L_{\rm diff}$ have been discussed in Section 3. The factor j_0 is determined by applying a least squares fit of Equation (7) to the observed intensities at the injection point $x = 0$ (at 03:00 UT 2004 February 15), which yields $j_0 = 10{,}430\,{\rm cm}^{-2}\,{\rm s}^{-1}\,{\rm sr}^{-1}\,{\rm MeV}^{-1}$.

Figure 4 shows the evolution of the particle differential intensity spectra, which are color coded by time after injection. The observed intensities are shown by solid dots, and the theoretical intensities (7) by solid lines. We choose eight instances for the spectral analysis: 0, 15, 45, 60, 80, 100, 120, and 140, all in hours after the injection time. The four later-time (80, 100, 120, and 140 hr) spectra for both observational and theoretical results are multiplied by a factor of 100, and 45 hr case by a factor of 0.6 for presentation purposes. A power-law spectrum with an index of -1.5 is displayed for reference since the observed interplanetary shock has compression ratio of $r = 2.5$, giving a DSA power-law index of $-3r/(r-1) = -5.0$ for the particle distribution function, or -1.5 for the differential intensity.

Table 1 shows the corresponding times (UT) and the normalized distances, $x/L_{\rm diff}$, for these eight instances. We apply power-law fitting to both the model and data at each selected time. Approximate power-law indices are obtained and listed in Table 1. The particle spectra harden with increasing distance from the injection point. The observed early-time spectra are a little harder than the DSA spectrum, and the late-time spectra are clearly flatter. This feature is well reproduced by our theoretical solution. However, like the flux amplification in Figure 3, our predicted spectra do not fit well with early-time

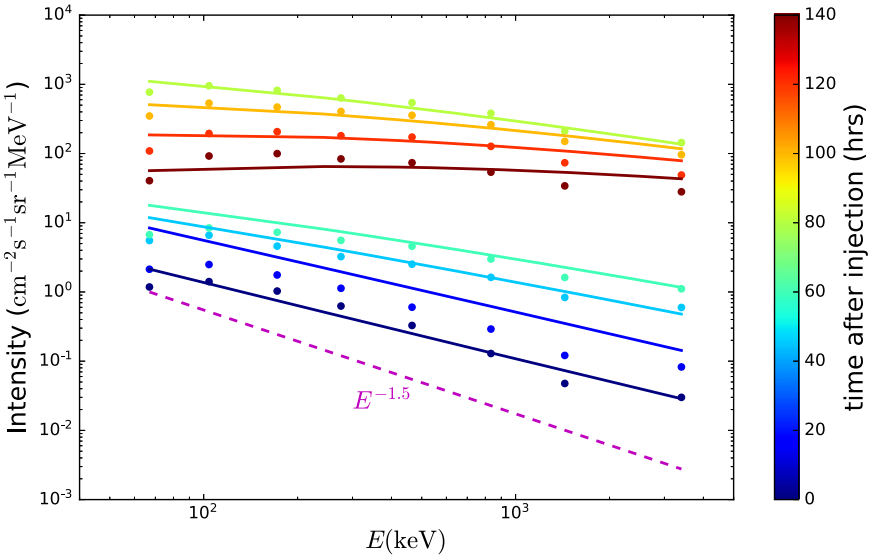

Figure 4. Evolution of the differential intensity spectrum. Solid dots denote observed particle intensities and solid lines the theoretical solutions. Both observational data and theoretical solutions are color coded by the time after the injection point (03:00 UT 2004 February 15). We choose eight instances for the spectral analysis: 0, 15, 45, 60, 80, 100, 120, and 140, all in hours after the injection time. Both observational and theoretical results for the last four cases (80, 100, 120, and 140 hr) are multiplied by a factor of 100, and the 45 hr case by 0.6 for presentation purposes. A power-law spectrum with an index of −1.5 is displayed for reference.

Table 1
Spectral Analysis for the Eight Selected Times

Time after Injection (hr)	Time (UT)	$\frac{x}{L_{\rm diff}}$	Theoretical Spectral Index	Observed Spectral Index
0	03:00 02/15	0	−1.09	−1.08
15	18:00 02/15	8.75	−1.03	−0.96
45	00:00 02/17	26.25	−0.82	−0.64
60	15:00 02/17	35	−0.69	−0.53
80	11:00 02/18	46.67	−0.53	−0.48
100	07:00 02/19	58.33	−0.37	−0.39
120	03:00 02/20	70	−0.22	−0.28
140	23:00 02/20	81.67	−0.07	−0.22

observations (i.e., the 15 hr case, $x/L_{\rm diff} \sim 0$–25). Nevertheless, the results are in rather good agreement in terms of the evolving spectral slope. At late times (∼140 hr), our model predicts a harder spectrum than observed, in part because the current model does not restrict the highest energy to which a particle can be accelerated.

6. Summary

The Z2014 kinetic transport theory for stochastic particle acceleration via reconnection processes in the solar wind has been extended to finite spatial regions by introducing an escape term. As in Z2014, we obtain power-law-like solutions for particle speeds, v, greater than the injection speed, v_0, with an index that depends on the dimensionless anti-reconnection electric field parameter, M_E, the ratio of particle diffusion to island contraction timescales, τ_d/τ_c, and the ratio of particle diffusion to particle escape timescales, τ_d/τ_e. Steeper power-law spectra result from a larger ratio τ_d/τ_e or a smaller τ_d/τ_c with a fixed M_E.

We present *Ulysses* LEMS30 observations showing an unusual enhancement of energetic particle fluxes downstream of an interplanetary shock at ∼5.4 au. The enhancement is inconsistent with predictions of classical DSA theory but can be explained by particle acceleration associated with small-scale magnetic island dynamics. Specifically, this work provides the first quantitative comparison of a theoretical prediction of the "time-intensity" profiles and evolving spectra of charged particles accelerated via a first-order stochastic reconnection associated mechanism with an atypical energetic particle (AEP) event. Our model reproduces the flux amplification and spectrum evolution reasonably well. It is also the first time that small-scale flux ropes were systematically detected via the GS reconstruction technique from *Ulysses* data near 5 au. Finally, we expect that our general theory of stochastic particle acceleration via magnetic reconnection processes, including particle injection, trapping, and escape, can explain other AEP events.

We thank the University of Helsinki for providing the Heliospheric Shock Database (http://ipshocks.fi/database). We acknowledge the partial support of the NSF EPSCoR RII-Track-1 Cooperative Agreement OIA-1655280, NSF-DOE award 1707247, NASA grants NNX08AJ33G, Subaward 37102-2, NNX14AC08G, NNX14AJ53G, A99132BT, RR185-447/4944336, and NNX 12AB30G. G.P.Z. is partly supported by the International Space Science Institute (ISSI), both through the award of the 2017 Johannes Geiss Fellowship and in the framework of an International Team Project 504 entitled "Current Sheets, Turbulence, Structures and Particle Acceleration in the Heliosphere." Y.C. and Q.H. acknowledge partial support from SAO subcontract SV4-84017 and NASA grants NNX15AI65G and NNX17AB85G.

ORCID iDs

L.-L. Zhao https://orcid.org/0000-0002-4299-0490
G. P. Zank https://orcid.org/0000-0002-4642-6192
O. Khabarova https://orcid.org/0000-0002-3230-2033
S. Du https://orcid.org/0000-0003-1134-3909
L. Adhikari https://orcid.org/0000-0003-1549-5256
Q. Hu https://orcid.org/0000-0002-7570-2301

References

Adhikari, L., Zank, G. P., Hunana, P., et al. 2017, ApJ, 841, 85
Ambrosiano, J., Matthaeus, W. H., Goldstein, M. L., & Plante, D. 1988, JGR, 93, 14383
Bieber, J. W., Wanner, W., & Matthaeus, W. H. 1996, JGR, 101, 2511
Bryant, D. A., Cline, T. L., Desai, U. D., & McDonald, F. B. 1962, JGR, 67, 4983
Chian, A. C.-L., & Muñoz, P. R. 2011, ApJL, 733, L34
Dmitruk, P., Matthaeus, W. H., & Seenu, N. 2004, ApJ, 617, 667
Drake, J. F., Swisdak, M., Che, H., & Shay, M. A. 2006a, Natur, 443, 553
Drake, J. F., Swisdak, M., & Fermo, R. 2013, ApJL, 763, L5
Drake, J. F., Swisdak, M., Schoeffler, K. M., Rogers, B. N., & Kobayashi, S. 2006b, GeoRL, 33, L13105
Greco, A., Matthaeus, W. H., Servidio, S., Chuychai, P., & Dmitruk, P. 2009, ApJL, 691, L111
Sonnerup, B. U. Ö, & Guo, M. 1996, GeoRL, 23, 3679
Hau, L.-N., & Sonnerup, B. U. Ö 1999, JGR, 104, 6899
Hietala, H., Eastwood, J. P., & Isavnin, A. 2014, PPCF, 56, 064011
Hoshino, M. 2012, PhRvL, 108, 135003
Hu, Q. 2017, Science China Earth Sciences, 60, 1466
Hunana, P., & Zank, G. P. 2010, ApJ, 718, 148
Khabarova, O., Zank, G. P., Li, G., et al. 2015a, ApJ, 808, 181
Khabarova, O. V., & Zank, G. P. 2017, ApJ, 843, 4
Khabarova, O. V., Zank, G. P., Li, G., et al. 2015b, JPhCS, 642, 012033
Khabarova, O. V., Zank, G. P., Li, G., et al. 2016, ApJ, 827, 122
Khabarova, O. V., Zank, G. P., Malandraki, O. E., et al. 2017, SunGe, 12, 23
Le, A., Karimabadi, H., Egedal, J., Roytershteyn, V., & Daughton, W. 2012, PhPl, 19, 072120
le Roux, J. A., Zank, G. P., Webb, G. M., & Khabarova, O. 2015, ApJ, 801, 112
le Roux, J. A., Zank, G. P., Webb, G. M., & Khabarova, O. V. 2016, ApJ, 827, 47
Matthaeus, W. H., Ambrosiano, J. J., & Goldstein, M. L. 1984, PhRvL, 53, 1449
Matthaeus, W. H., Bieber, J. W., Ruffolo, D., Chuychai, P., & Minnie, J. 2007, ApJ, 667, 956
Matthaeus, W. H., Goldstein, M. L., & Roberts, D. A. 1990, JGR, 95, 20673
Matthaeus, W. H., Smith, C. W., & Bieber, J. W. 1999, in AIP Conf. Ser. 471, Correlation lengths, the Ultrascale, and the spatial structure of interplanetary turbulence, ed. S. T. Suess et al. (Melville, NY: AIP), 511
Neugebauer, M., Giacalone, J., Chollet, E., & Lario, D. 2006, JGRA, 111, A12107
Oka, M., Phan, T.-D., Krucker, S., Fujimoto, M., & Shinohara, I. 2010, ApJ, 714, 915
Reames, D. V. 1995, RvGeo, 33, 585
Servidio, S., Matthaeus, W. H., Shay, M. A., et al. 2010, PhPl, 17, 032315
Servidio, S., Matthaeus, W. H., Shay, M. A., Cassak, P. A., & Dmitruk, P. 2009, PhRvL, 102, 115003
Teh, W.-L., Sonnerup, B. U. Ö, Hu, Q., & Farrugia, C. J. 2009, AnGeo, 27, 807
Tessein, J. A., Matthaeus, W. H., Wan, M., et al. 2013, ApJL, 776, L8
Tessein, J. A., Ruffolo, D., Matthaeus, W. H., et al. 2015, ApJ, 812, 68
Tessein, J. A., Ruffolo, D., Matthaeus, W. H., & Wan, M. 2016, GeoRL, 43, 3620
Zank, G. P., Adhikari, L., Hunana, P., et al. 2017, ApJ, 835, 147
Zank, G. P., Hunana, P., Mostafavi, P., et al. 2015, ApJ, 814, 137
Zank, G. P., le Roux, J. A., Webb, G. M., Dosch, A., & Khabarova, O. 2014, ApJ, 797, 28
Zank, G. P., & Matthaeus, W. H. 1992, JGR, 97, 17189
Zank, G. P., & Matthaeus, W. H. 1993, PhFl, A5, 257
Zhao, L.-L., Adhikari, L., Zank, G. P., Hu, Q., & Feng, X. S. 2017, ApJ, 849, 88
Zhao, L.-L., Adhikari, L., Zank, G. P., Hu, Q., & Feng, X. S. 2018, ApJ, 856, 94
Zheng, J., & Hu, Q. 2018, ApJL, 852, L23